Check for updates

Fabrication of a ZnFe$_2$O$_4$@Co/Ni-MOF nanocomposite and photocatalytic degradation study of azo dyes

Khalid Javed,[a] Naseem Abbas,[a] Muhammad Bilal,[a] Abdulaziz A. Alshihri,[b] Hafiza Zahra Rab Nawaz,[c] Mohamed Fawzy Ramadan[d] and Syed Ali Raza Naqvi [iD] *[c]

This study addresses the critical issue of removing organic pollutants from water, focusing on the photocatalytic degradation of Congo red (CR) dye using a novel ZnFe$_2$O$_4$@Co–Ni metal–organic framework (MOF) nanocomposite (ZFCNM). The primary aim was to develop a photocatalyst with enhanced efficiency by combining the properties of ZnFe$_2$O$_4$ with Co/Ni-MOF, leading to a low band gap (2.89 eV) and a high surface area (723 m^2 g^{-1}). The ZFCNM nanocomposite, synthesized *via* a hydrothermal method, was characterized by X-ray diffraction (XRD) and field emission scanning electron microscopy (FESEM), confirming the formation of face-centered cubic ferrite and hexagonal MOF structures. Fourier-transform infrared spectroscopy (FTIR) verified the presence of carboxyl (–COOH) groups and Fe–O bonds in the composite. Photodegradation efficiency was evaluated under varying conditions, including reaction time, pH, catalyst dosage, contaminant concentration, and light intensity. The ZFCNM photocatalyst, with an equal mass ratio of Co/Ni-MOF and ZnFe$_2$O$_4$, achieved a 98% removal efficiency of CR (75 min reaction time, pH 5, at 25 °C, and visible-light intensity of a 50 W LED lamp) significantly outperforming Co/Ni-MOF (24%) and ZnFe$_2$O$_4$ (36%) alone. The estimated quantum yield (QY) was 3.00×10^{-6} molecules per photon, and kinetic studies revealed a first-order reaction pathway with an R^2 value of 0.9813. These results highlight the potential of ZFCNM as an effective photocatalyst for water purification applications.

1. Introduction

Water is equally important to life as oxygen and needs to be purified. Of total water resources, 3% is freshwater of which 1.2% is available for drinking, and 1.8% is locked up in ice caps, glaciers and permafrost or buried deep in the earth. Out of the 1.2% of available drinking water, only 0.5% is now drinkable. The remaining 0.7% has become polluted due to human activities, which could lead to adverse health effects.[1] Today, water pollution is a global issue. In his poem, James Casey reflects on this situation by saying, "*Water water everywhere and not a drop to drink*". Human activities and social needs are playing a triggering role in polluting waterbeds. Among the complex water pollutants are dyes, especially CR azo dyes. These dyes satisfy the human aesthetic sense as coloring agents in various industries, such as paper, textiles, paints, leather, and food. However, they are also carcinogenic, mutagenic, and teratogenic in nature.[2–5] The elimination or fixation of dyes and related compounds from waterbeds could stop their widespread transfer through water cycles to animals and humans. Due to their stability and complex structure, it is a difficult task to eliminate or fix them from natural water cycles.[6]

Numerous studies have been conducted to explore diverse methods for addressing organic pollutants in water, including membrane separation processes,[7] advanced oxidation processes (AOPs),[8,9] adsorption,[10] biofiltration,[11] photocatalytic degradation,[12] ozonation,[13] bio-degradation,[14] sono-degradation,[15] chlorination,[16] heterogeneous catalysis,[17] and activated carbon treatment.[18] Due to its easy handling, cost-effectiveness, and higher removal efficiency, photodegradation has emerged as a highly efficient and significant technique for eliminating pollutants from water[19] using a variety of catalysts. Degradation efficiency is significantly influenced by factors such as catalyst type, composition, and operational parameters. For the remediation of organic pollutants, several kinds of materials are currently being used, including inorganic nanomaterials, such as metals/metal oxides, metals/metal sulfides, and nanomaterials based on carbon structures.[18,20–22] Additionally, nanomaterials derived from organic molecules like metal–

[a]Institute of Chemical Sciences, Bahauddin Zakariya University, Multan 60800, Punjab, Pakistan

[b]Department of Radiological Sciences, College of Applied Medical Sciences, King Khalid University, Abha, Saudi Arabia

[c]Department of Chemistry, Government College University Faisalabad, Faisalabad-38040, Punjab, Pakistan. E-mail: draliraza@gcuf.edu.pk; Tel: +92-313-9904742

[d]Department of Clinical Nutrition, Faculty of Applied Medical Sciences, Umm Al-Qura University, Makkah, Saudi Arabia

organic frameworks (MOFs), nano-membranes, and organic polymers are also being utilized.[23,24] Composite materials with their larger surface area are much better and more effective for getting rid of pollutants in water.

Currently, semiconductor-based nanostructures are used as photocatalysts and are active in the UV region.[25] In photocatalysis, the design and development of photocatalysts active in the visible areas is an attention-grabbing topic for a safe environment.[26] Ferrites are used in developing viable technological devices due to their exciting electrical domain, fascinatingly active magnetic properties, and structure.[27,28] $ZnFe_2O_4$ (ZF) is one of the most important spinel ferrites. It has proven very useful in various applications, such as highly sensitive contrast agents in MRI,[29] gas sensors,[30] ethanol sensors,[31] acetone sensors,[32] as an anode material for LIBs,[33] and for the photocatalytic breakdown of organic pollutants.[34,35] Because of its chemical stability characterized by a visible light band gap of 1.92 eV, ZF has gained attention for application in solar cells.[36,37] Its reduced surface area has constrained its effectiveness in the photodegradation of organic pollutants found in wastewater, such as dyes.

Within advanced oxidation processes (AOPs) like photocatalysis and Fenton reactions, MOFs have arisen as innovative agents for eliminating organic pollutants.[38] This is attributed to their unique characteristics, including a high surface area, optimized specific active sites that foster the adsorption and degradation of contaminants, and inherent cavities that facilitate host–guest interactions. Additionally, their structural adaptability for selective adsorption and catalysis, along with exceptional water stability, further enhance their effectiveness.[39] The choice of the complex ZF@cobalt/nickel-MOF (ZFCNM) structure was driven by its synergistic properties, combining the high surface area and selective adsorption capabilities of MOFs with the low band gap and visible light activity of ZF. This combination aims to enhance photocatalytic efficiency and improve performance in dye degradation, offering a more effective solution for wastewater treatment compared to simpler structures. Therefore, the fabrication of ZF with MOFs could be an efficient composite photocatalyst due to efficient adsorption and photocatalytic degradation.

The current study presents a novel approach in the synthesis of a ZF@cobalt/nickel-MOF (ZFCNM) nanocomposite with a high surface area and low band gap through a facile hydrothermal process. This work stands out for its innovative combination of ZF with MOFs, leveraging the unique properties of both materials to enhance photocatalytic performance in the visible region. This research demonstrates a significant advance in the effective degradation of CR dye under visible light, optimized through pH, catalyst dosage, light intensity, and exposure time. The photodegradation mechanism of CR on ZFCNM was also studied based on kinetics and a radical scavenger test. The performance evaluation of ZFCNM for the photodegradation of CR was also compared with some literature reports based on quantum yield (QY) and space-time yield (SY). The prepared ZFCNM also offers potential for multiple reuse and easy recovery due to its heterogeneous nature. These findings contribute new insights into the development of high-performance photocatalysts for wastewater

treatment, addressing the limitations of conventional ferrite-based materials.

2. Experimental

2.1 Materials

The present study employed analytical grade chemicals with purity exceeding 99%. Trimesic acid, polyvinylpyrrolidone (PVP), dimethyl formamide (DMF), $Fe(NO_3)_3 \cdot 9H_2O$, $Zn(NO_3)_2 \cdot 6H_2O$ $Ni(NO_3)_2 \cdot 6H_2O$, and $Co(NO_3)_2 \cdot 6H_2O$ were utilized. Ethanol (C_2H_5OH) and sodium hydroxide (NaOH) were of analytical grade. All chemicals were purchased from Merck and Sigma Aldrich. Double-deionized (DDI) water was employed to prepare sample solutions.

2.2 Synthesis of $ZnFe_2O_4$ nanoparticles

ZF nanoparticles were synthesized *via* the co-precipitation method. $Fe(NO_3)_3 \cdot 6H_2O$ (0.2 M) was dissolved separately in 100 mL of water to get a homogenous solution *via* gentle stirring. Separate solutions of $ZnNO_3 \cdot 6H_2O$ (0.1 M) and $Fe(NO_3)_3 \cdot 6H_2O$ (0.2 M) were prepared in 100 mL of water each, achieving a homogeneous solution through gentle stirring. The prepared solutions were mixed dropwise simultaneously with continuous stirring. To maintain pH 10, NaOH (2 M) solution was added dropwise. Following the successful mixing of the solutions to achieve the desired pH, the temperature of the mixture was elevated to 80 °C and consistently maintained at this level for 3 hours. This controlled heating process persisted until the formation of brown precipitates. The generated precipitates underwent centrifugation, after which they were subjected to thorough washing using deionized water (DI) and ethanol (C_2H_5OH). This meticulous washing persisted until all unreacted substances were effectively removed from the precipitates. Subsequently, the obtained precipitates were subjected to drying within a hot-air oven set at a temperature of 75 °C for 24 hours to ensure the complete removal of moisture from the precipitates. The ZF nanoparticles were attained by calcining the dried precipitates at 600 °C for 6 h and used for preparing ZFCNM composites.

2.3 Preparation of ZFCNM composite

The cobalt/nickel-metal organic framework (CNM) was synthesized using a standard procedure with some modifications.[40] Weighed quantities of trimesic acid (2 mmol), $Co(NO_3)_2 \cdot 6H_2O$ (1 mmol), $Ni(NO_3)_2 \cdot 6H_2O$ (1 mmol), and polyvinylpyrrolidone (PVP) (2 mmol) were dissolved in a 14 mL mixture of $H_2O : DMF$ (1 : 6 v/v). To this solution, 0.167 g of synthesized ZF was introduced. The reaction mixture was placed within a Teflon autoclave and heated to 80 °C for 1 hour. Subsequently, the autoclave was transferred to an oven and maintained at 120 °C for three days. Then, the mixture was allowed to cool to room temperature. The resultant material was thoroughly washed using water and DMF, employing centrifugation to facilitate separation. The washed material was subsequently dried in a hot-air oven at 110 °C overnight to eliminate any residual moisture.

2.4 Characterization tools

The structural characteristics and elemental composition of the prepared materials were assessed using FESEM combined with EDX using a Nova Nano FE-SEM 450 model. The grain size distribution of ZF, CNM, and the composite ZFCNM was determined from FESEM images utilizing ImageJ software. Attenuated total reflectance-Fourier transform infrared (ATR-FTIR) spectra were acquired using a Bruker ATR-FTIR-8400S spectrophotometer to gain insights into molecular vibrations and structural information. Crystallinity and phase analysis of the materials were studied using XRD spectroscopy with a Bruker D8 Advance X-ray Powder Diffractometer, applying Cu Kα radiation ($\lambda = 1.5406$ nm). The analysis spanned a 2θ range of 10–$70°$ with a step size angle of $0.01975°$. Optical characteristics, including band gap energy, of ZF, CNM, and ZFCNM were determined through UV-visible diffuse reflectance spectroscopy (DRS) analysis. This was accomplished using a HACH (DR-6000) spectrophotometer at room temperature, employing the Tauc equation (eqn (1)):

$$\alpha\hbar\nu = \beta(\hbar\nu - E_g)^n \tag{1}$$

where α is the absorption coefficient, $\hbar$ is Plank's constant, ν is the vibration frequency, and E_g (eV) is the energy band gap, while the "n" exponent is the type of transition and is equal to either $\frac{1}{2}$ or 2 for a direct band gap or an indirect band gap energy, respectively. The textural features (*e.g.*, pore volume, pore size distribution, and specific surface area) of synthesized ZF, CNM, and ZFCNM materials were determined through analysis of the N_2 adsorption–desorption isotherms with the aid of the Brunauer–Emmett–Teller (BET) and the Barrett–Joyner–Halenda (BJH) model theories using Quantachrome (Autosorb-iQ-MP/XR) apparatus.

2.5 Photocatalytic degradation of CR dye solution

The photocatalytic efficiency in degrading CR dye (10 mg L^{-1}) by ZF, CNMF, and ZFCNM was assessed under visible light exposure, utilizing a 50 watt (W) LED lamp. This assessment dispersed 0.01 g of the synthesized ZF, CNMF, or ZFCNM photocatalyst in a 100 mL solution containing CR dye (10 mg L^{-1}). The suspension was initially placed in darkness on a mechanical shaker, operating at 15 rpm and ambient temperature, for 90 minutes to attain adsorption equilibrium. The pH of the solution was maintained at 7.0. Following the adsorption equilibrium phase, the suspensions were subjected to visible light irradiation from a 50 W LED lamp. This initiated the photodegradation process of the CR dye. At specific time intervals (15 minute increments), small portions of the solution (3 mL) were withdrawn from the suspensions. These samples were then centrifuged and analyzed using a UV-vis spectrophotometer (Shimadzu UV-1801) to quantify the percentage of CR dye removal, assessing both the adsorption and photocatalytic processes (as per eqn (2)):

$$\text{Removal } (\%) = \frac{C_0 - C_t}{C_0} \times 100 \tag{2}$$

where C_0 is the concentration of CR dye before removal, and C_t is the concentration of CR dye solution after removal at time t (min), respectively.

2.6 Effect of operating variables on the photocatalytic activity

The one factor at a time (OFAT) method was followed to investigate and optimize the effect of operating variables on the photocatalytic activity of ZFCNM against CR dye removal. The operating variables were: solution pH (5–11), reaction time (15–90 min), pollutant (CR) concentration (10–20 mg L^{-1}), catalyst dose (0.25–1 g L^{-1}), and visible light intensity (25–50 W). The photocatalytic degradation efficiency of ZFCNM (1 g L^{-1} dose) against CR dye (10 mg L^{-1}) as a function of time (15–90 min) was investigated at neutral pH using visible light (25 and 50 W) intensity. The effect of pH in the range of (5–11) on the photocatalytic activity of ZFCNM against CR dye (10 mg L^{-1}) removal was optimized by keeping the following conditions fixed: catalyst dose 1 g L^{-1}, light intensity 50 W, irradiation time 75 min. The dose of the catalyst (0.25–1 g L^{-1}) was optimized against the removal of 10 mg L^{-1} CR dye solution while keeping the other conditions fixed as follows: pH 5.0, light intensity 50 W, irradiation time 75 min. Using a dose of 1.0 g L^{-1} of ZFCNM, the effect of CR dye concentration (10, 15, and 20 mg L^{-1}) on the photocatalytic performance was also investigated at pH 5.0 using a light intensity 50 W for 75 minutes of irradiation.

2.7 Performance evaluation

To understand the practical merits of photocatalytic systems, the performance evaluation of different photocatalysts for abatement of CR was evaluated by energy consumption during catalysis. For this purpose, QY, SY, energy consumption, and figure of merit (FOM) were calculated using eqn (3)–(6):[41]

$$\text{SY} = \frac{\text{QY (molecules per photon)}}{\text{Photocatalyst mass (mg)}} \tag{3}$$

$$\text{QY} = \frac{\text{decay rate (molecules per second)}}{\text{photon flux (molecules per second)}} \tag{4}$$

$$\text{Energy consumption} = \frac{\text{lamp power (W)} \times \text{time (h)}}{\text{number of degraded polutants (}\mu\text{mol)}} \tag{5}$$

$$\text{FOM} = \frac{\text{product obtained (L)}}{\text{catalyst mass (g)} \times \text{time (h)} \times \text{energy consumption }(\text{W h }\mu\text{mol}^{-1})} \tag{6}$$

2.8 Kinetic studies

The degradation of CR dye in the presence of the photocatalyst was evaluated using zero-order, first-order, and second-order kinetic models, as expressed by eqn (7), (8), and (9), respectively. The examination of CR dye degradation involving the photocatalyst was conducted by applying three kinetic models: zero-order, first-order, and second-order. These kinetic models were mathematically defined by eqn (10), (11), and (12) for zero-order, first-order, and second-order kinetics, respectively.[42]

$$\frac{dc}{dt} = -k_0 \tag{7}$$

$$\frac{dc}{dt} = -k_1 C \tag{8}$$

$$\frac{dc}{dt} = -k_2 C_2 \tag{9}$$

where C is the concentration of CR; t is the reaction time, and k_0, k_1, and k_2 represent the apparent kinetic rate constants of the respective zero, first, and second-order reaction kinetics. Eqn (10)–(12) resulted from the integration of eqn (7)–(9):[42]

$$C_t = C_0 - k_0 t \tag{10}$$

$$C_t = C_0 e - k_1 t \tag{11}$$

$$\frac{1}{C_t} = \frac{1}{C_0} + k_2 t \tag{12}$$

where C_t is the concentration of CR after irradiation time t.

2.9 Point of zero charge (PZC)

To determine the specific pH value exhibited by the nanocomposite and a neutral surface charge (referred to as pH_{pzc}), eight test tubes were prepared. Each tube contained 10 mL of a 0.01 M NaCl solution with pH levels ranging from 2 to 8. Subsequently, 0.03 g of the nanocomposite (CNMZF) with a 1:1 composition was introduced into each test tube. These tubes were then placed in a shaker operating at 250 rpm and maintained at 25 °C. After 48 hours, the pH of the sample was re-measured.

2.10 Radical scavenger and reusability test

Three scavengers were introduced during the optimized photocatalytic degradation of CR dye to identify the primary oxidative radical species generated by the ZFCNM composite. Four separate photocatalytic reaction vessels containing 10 ppm 50 mL pollutant solution containing 0.025 g of catalyst (ZFCNM) were prepared for the test. To scavenge the effective radical, 1 mM of disodium ethylenediamine tetra acetate (EDTA-2Na, as an inhibitor for positive holes (h^+), 1 mM of tertiary butyl alcohol (TBA, as an inhibitor for ˙OH radicals), and 1 mM benzoquinone (BQ, as an inhibitor for ˙O_2^- radical species), were added, separately. To proceed with the photocatalytic degradation, the reaction mixture was irradiated with visible light using a 50 W bulb for 90 minutes, and then the absorbance was measured at a wavelength of 498 nm to understand the role of the scavenger in degradation. To investigate the regeneration and repeated utilization of the catalyst, the employed photocatalyst was subjected to a washing process involving water and ethanol. Following the washing step, the catalyst was dried in an oven maintained at 105 °C for one hour. This regenerated catalyst was then employed for photocatalytic reactions under the same optimized conditions for six successive cycles.

3. Results and discussion

3.1 Evaluation of photocatalytic performance against CR dye removal

We observed that the CNMZF (1:1) composite effectively removed CR dye in the dark and in visible light, as shown in Fig. 1. It showed slightly better adsorption than bare CNM or ZF NPs in the dark. Increasing the ZF dopant mass by over 50% led to a small decrease in dye adsorption. Under visible light, bare ZF and CNM catalysts improved CR dye removal to 29.23% and 36.54%, respectively. Notably, CNMZF composites with CNM : ZF mass ratios of 1:2, 1:1, and 2:1 outperformed the bare catalysts, achieving 71.39%, 98.4%, and 80.51% CR dye degradation, respectively. These findings highlight that CNMZF (1:1) is a superior choice for CR dye removal in both dark and light conditions.

3.2 Characterization

The morphological features of the synthesized ZFCNM (1:1) composite (the top-performing photocatalyst) and bare ZF and CNM were observed by FESEM analysis and are shown in Fig. 2a–c. The well-defined crystalline rod-like 3D morphology of CNM (Fig. 2a) with no apparent impurities, uniform morphology of ZF granules (Fig. 2b), and successful synthesis of a flower-like ZFCNM nanocomposite heterostructure were observed along with agglomeration of ZF nanoparticles over the surface of flower-like CNM rods (Fig. 2c).
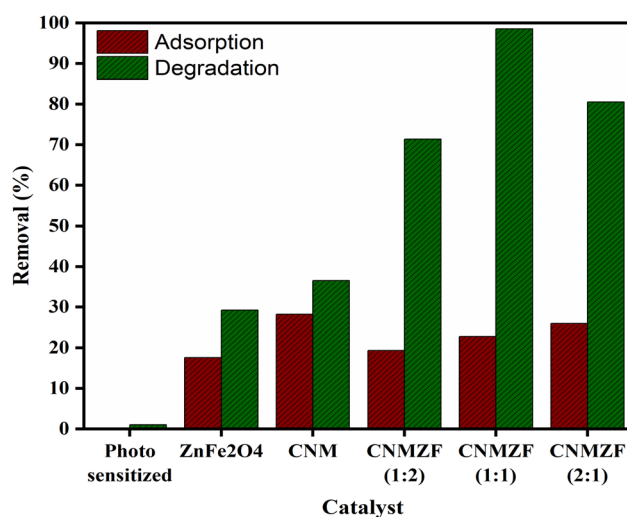

Fig. 1 Adsorption and photocatalytic removal of CR dye (10 mg L^{-1}) with different CNMZF compositions compared to bare photocatalysts, conducted under dark and visible light (50 W) conditions for 75 minutes.
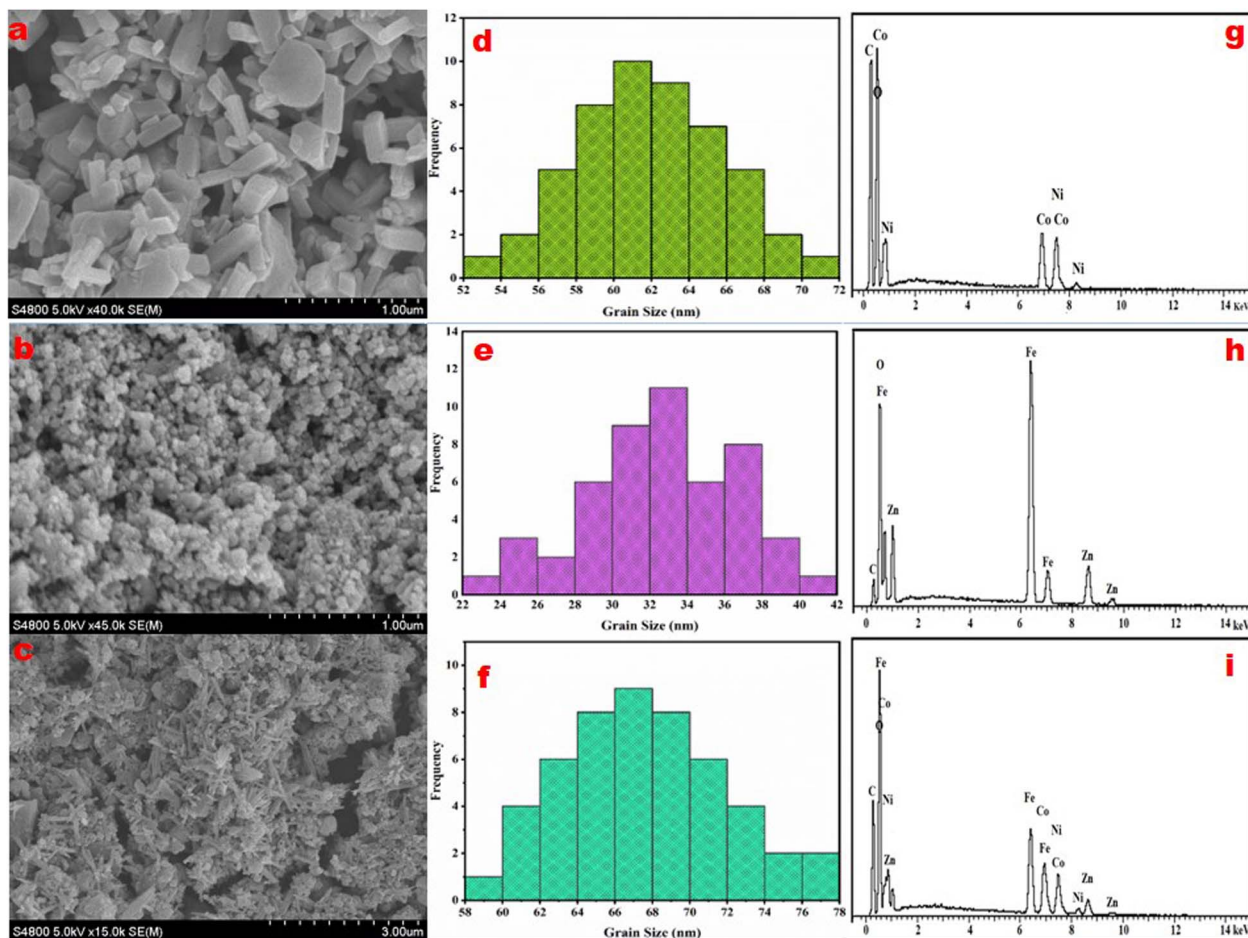
Fig. 2 FESEM images (a–c), histograms for grain size (d–f), and EDX (g–i) of synthesized samples (i) CNM, (ii) ZF, and (iii) ZFCNM.

Histograms show the average grain size distribution in the ranges 60–62, 32–34, and 66–68 nm for synthesized CNM (Fig. 2d), ZF (Fig. 2e), and ZFCNM (Fig. 2f), respectively. A slight increase in grain size of ZFCNM compared to that of CNM or ZF nanoparticles was observed.[43] The elemental composition with atomic percentages of CNM, ZF, and ZFCNM were determined by EDX and are shown in Table 1.

To evaluate the crystalline phases of the prepared materials, XRD patterns of the ZF, CNM, and ZFCNM (1 : 1) composite are given in Fig. 3. Typical diffraction peaks of CNM and ZF without a significant shift/alteration in their 2θ values can be seen in the

XRD pattern of the ZFCNM composite. The XRD pattern of ZF showed a typical face-centered cubic (FCC) structure with diffraction peaks at 2θ values of 30.07, 35.45, 43.13, 53.54, 57.02, and 62.73 in agreement with JCPDS card number 001-1109.[44] The corresponding crystal planes (320), (410), (422), (531), (541), and (710), respectively, are in agreement with JCPDS card number (001-1109). The typical peaks at 2θ values of 7.37, 10.99, 12.74, 14.74, 18.40, 22.45, 25.65, and 38.98 correspond to the presence of CNM crystals in the ZFCNM composite. The crystallite sizes (D, nm) of ZF and CNM before and after

Table 1 Comparison of the atomic percentage observed in the synthesized materials (EDX analysis) and theoretical values

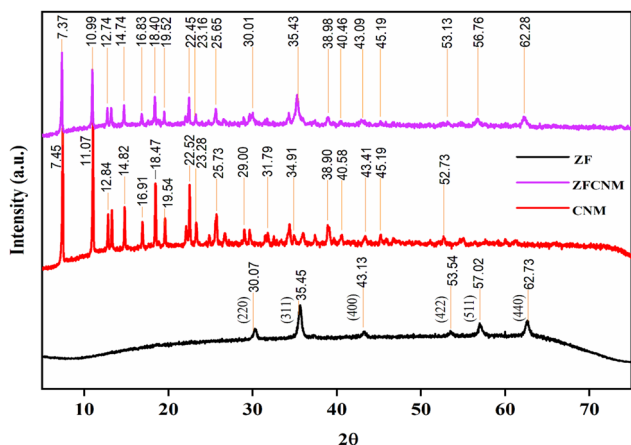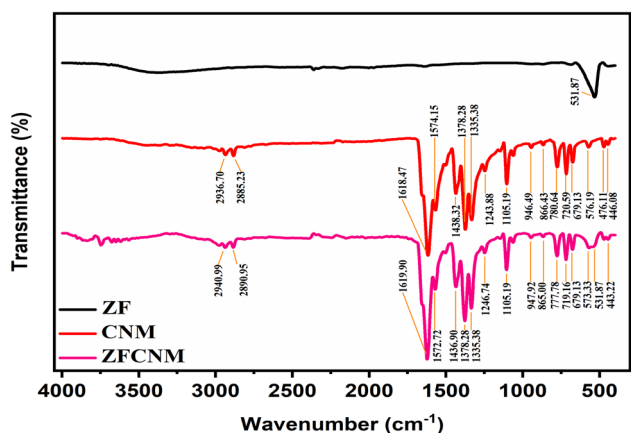| Atoms	ZF		CNM		ZFCNM	
	Observed values (atom%)	Theoretical values (atom%)	Observed values (atom%)	Theoretical values (atom%)	Observed values (atom%)	Theoretical values (atom%)
Zn K	12.41	14.28	—	—	1.81	2.17
Fe K	27.38	28.57	—	—	5.73	6.66
O K	56.32	57.14	42.62	26.08	41.97	33.33
Ni K	—	—	3.79	4.34	3.32	3.33
Co K	—	—	4.36	4.34	3.47	3.33
C K	—	—	49.19	39.13	43.7	30

Fig. 3 XRD spectra of ZF, CNM, and ZFCNM.

Fig. 4 FTIR spectra of synthesized ZF, CNM, and ZFCNM.

hybridization in the ZFCNM composite were calculated using the Debye–Scherrer formula (eqn (13)):[45]

$$D = \frac{(0.9\lambda)}{(\beta \cos \theta)} \qquad (13)$$

where θ, λ, and β are the diffraction angle, the wavelength of the X-ray source, and the full width at half-maximum intensity, respectively. Based on the Debye–Scherrer formula, the average crystallite sizes of bare ZF, CNM, and ZFCNM composite were calculated as 22.44, 58.61, and 64.65 nm *via* diffraction peaks located at 57.02°, 31.65°, and 22.45°, respectively.[46] The increase in crystal size in the composite is in agreement with the results given in the histograms.

The FTIR spectra of synthesized CNM, ZF, and their composite ZFCNM (1 : 1) heterostructure photocatalyst are depicted in Fig. 4. In the FTIR spectrum of CNM, the absorption peaks at 1618, 1483, and 1378 cm^{-1} were attributed to the asymmetric and symmetric vibrational bands corresponding to the carboxylate functional group (–COOH) within the trimesic acid ligand present in CNM. Peaks at 2936 and 2885 cm^{-1} were assigned to the asymmetric C–H alkane stretching and O–H carboxyl acid stretching, respectively.[47] The 1105 and 1243 cm^{-1} peaks were attributed to the stretching vibration of the C–O bond within the uncoordinated free carboxyl group on the MOF surface.[32] Peaks at 946 and 576 cm^{-1} were linked to the CH$_2$ rocking and bending of N–C=O, respectively.[48] Furthermore, the peaks at 780 and 719 cm^{-1} were attributed to the out-of-plane bending vibration of C–H, while the peaks at 1335 and 866 cm^{-1} were associated with the stretching vibration of aromatic C=C and alkene C=C bonds, respectively. The prominent and broad absorption band observed at 532 cm^{-1} corresponds to the distinctive feature of spinel ferrites, signifying the M-O stretching vibrations present in both tetrahedral and octahedral sites within the ZF component of the ZFCNM composite.[49] Notably, none of the primary peaks detected in
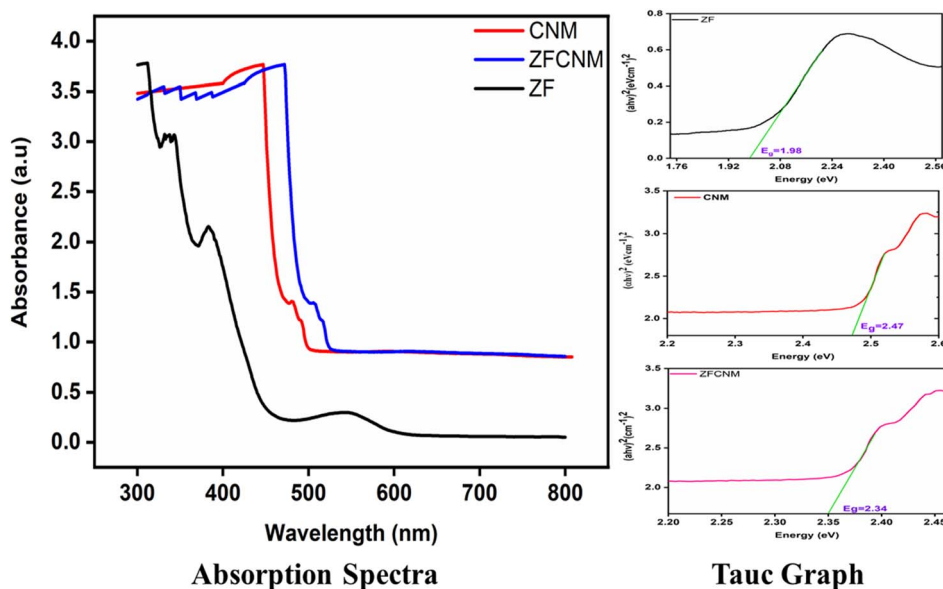

Fig. 5 The UV-visible DRS spectra and Tauc graphs of synthesized (a) ZF, (b) CNM, and (c) ZFCNM.

CNM exhibited any alteration, implying that the fundamental chemical structure of CNM remained unaffected. Notably, the primary peaks observed in the CNM spectrum are also present in the ZFCNM composite without significant shifts or changes in intensity. This indicates that the fundamental chemical structure of CNM remains intact within the composite, confirming that the formation of the ZFCNM composite does not alter the basic framework of CNM.

The optical features and band gap energy of synthesized ZF, CNM, and ZFCNM (1 : 1) composite structures were compared based on their UV-visible DRS spectra, as shown in Fig. 5. The spectra obtained for all the prepared materials exhibited a broad absorption pattern within the UV-visible range. The UV-visible, diffuse reflectance spectroscopy (DRS) analysis confirmed the enhancement in absorption characteristics brought about by the combination of ZF with CNM, forming the ZFCNM composite. Notably, compared to pristine CNM, the ZFCNM composite displayed a notable blue shift in the absorption band edge, shifting from 508 nm to 532 nm, signifying improved visible light absorption. The improved photodegradation efficiency suggests effective electron–hole pair separation due to optimized band alignment. Utilizing the Tauc formula, the calculated band gap energy (E_g) values for the synthesized materials were determined as follows: ZF 1.98 eV, CNM 2.47 eV, and ZFCNM 2.34 eV. These findings strongly suggest that incorporating ZF within the porous framework of CNM enhances both the optical response and photocatalytic capabilities, particularly under the broader range of UV-visible light irradiation and in agreement with previously reported work. Ramezanalizadeh and Manteghi reported Eg values of synthesized MOF 2.5 eV, BiFeO₃ 2.1 eV and MOF/BiFeO₃ 2.3 eV.[46] Bilal *et al.* reported Eg values for synthesized CuF, Co-MOF, and CuF@CM of 2.0, 2.4 and 2.2 eV, respectively.[43]

The textural features (porosity and specific surface area) of ZF, CNM crystals, and their hybrid ZFCNM (1 : 1) nanocomposite were evaluated based on the N₂ adsorption–desorption isotherms presented in Fig. 6. The N₂ adsorption behavior
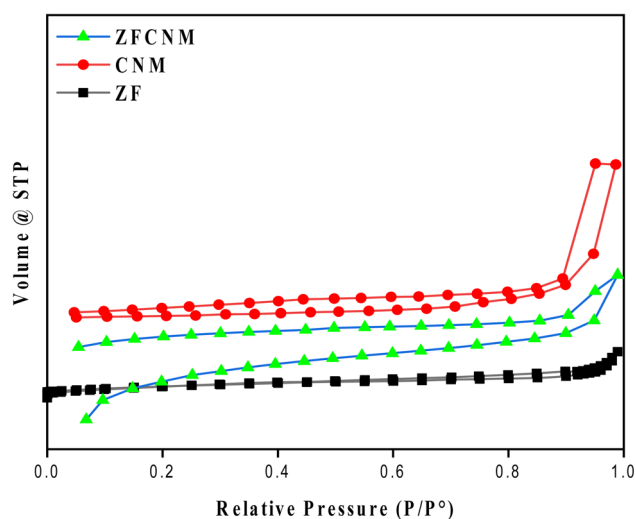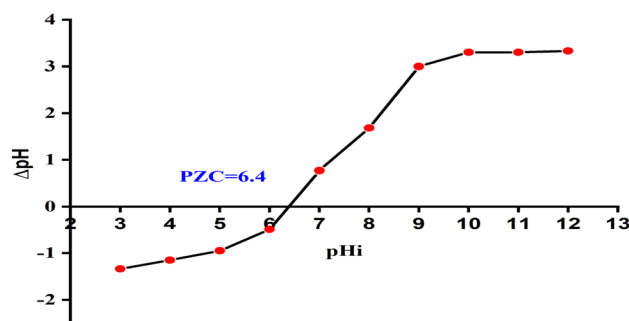

Fig. 7 pH (pzc) of CNMZF (1 : 1).

of CNM and the ZFCNM composite is comparable with a type-I adsorption isotherm, which is attributed to the microporous nature of the prepared materials based on the IUPAC classification. Based on the BET analysis, ZF showed a specific surface area of 3.14 m² g⁻¹, whereas CNM had a specific surface area of 798 m² g⁻¹, with an average pore size of 1.96 nm and pore volume of 0.39 cm³ g⁻¹. Comparatively, it was noteworthy that the immobilization of CNM with ZF diminished the specific surface area of the ZFCNM composite to 723 m² g⁻¹. In contrast, the ZFCNM composite showed an increase in the average pore diameter (2.32 nm) and pore volume (0.43 cm³ g⁻¹) compared with bare CNM.

3.3 PZC measurement

The findings clearly indicate that the pH$_{pzc}$ of the CNMZF (1 : 1) nanocomposite is around 6.4, as shown in Fig. 7. This result provides a precise understanding of how the surface charge of the nanocomposite responds to changes in pH.

3.4 Photocatalytic degradation of CR dye

The effect of real polluted water conditions on the photocatalytic efficiency of the synthesized material was optimized.

3.4.1 Effect of time. Time is the key factor in defining the kinetics of degradation by a catalyst. Fig. 8a demonstrates the photocatalytic degradation of CR dye by ZFCNM (1 : 1) over time. Initially, the degradation rate increased significantly, reaching 73% within 75 minutes, due to the high concentration of reactants and effective light penetration, which allowed the catalyst to be highly active. However, beyond this point, the degradation rate plateaued. This plateau can be attributed to several factors: the reduced concentration of the reactant, the accumulation of degradation byproducts leading to solution turbidity hindering light penetration, and the saturation of the catalyst's active sites, all of which limit further degradation.[50]

3.4.2 Effect of solution pH. Fig. 8b depicts the influence of solution pH on the photocatalytic degradation efficiency of the ZFCNM (1 : 1) composite against CR dye. Notably, the optimal catalytic photodegradation occurred under acidic conditions (pH = 5), with degradation efficiency diminishing as the alkalinity gradually increased. The heightened photocatalytic degradation efficiency observed under acidic conditions can be attributed to the dipolar nature of the anionic CR dye and the
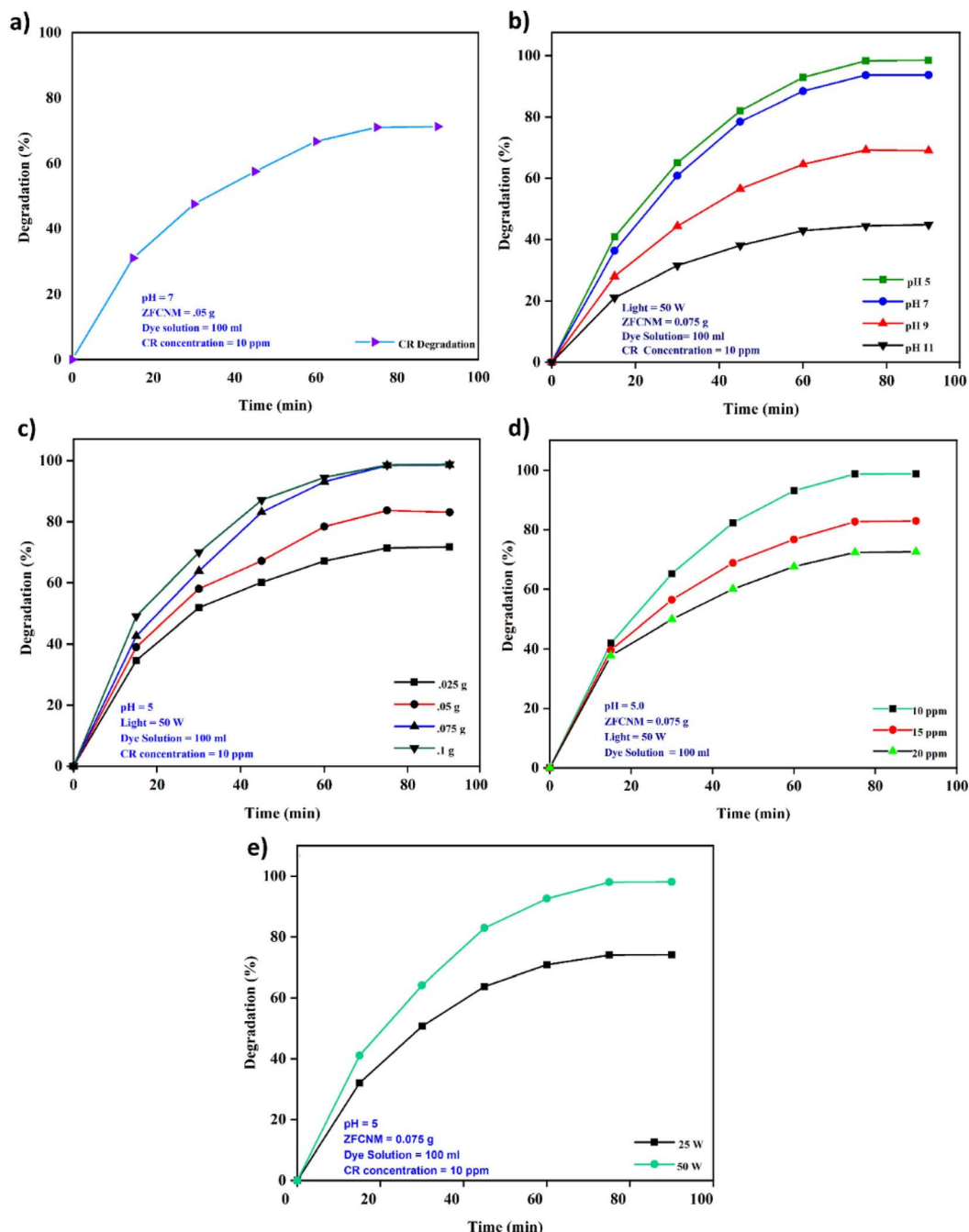

Fig. 6 BET isotherms of ZF, CNM, and ZFCNM.

Fig. 8 Effects of different variables, (a) time, (b) pH, (c) catalyst dose, (d) contaminant concentration, and (e) light intensity, on the removal efficiency of ZFCNM against CR.

electrostatic forces of attraction between the dye molecules and the catalyst surfaces. It is important to note that the particular composition of the photocatalyst influences the nature of available surface charges.[41] Changes in pH can potentially modify the surface charge of the catalyst and affect the dissociation of the anionic dye. This phenomenon is due to the presence of protons in an acidic medium, influencing the chemical state of the dye within the solution and the functional groups present on the adsorbent surface at a specific pH level.[51] As the pH increases beyond the pH_{pzc} (6.4), the surface of the

catalyst becomes more negatively charged, leading to a reduction in electrostatic attraction and thus a decline in degradation efficiency. This behavior underscores the importance of pH in optimizing photocatalytic activity, as it directly influences the surface charge of the catalyst and its interaction with dye molecules. The findings provide valuable insights into how pH manipulation can be used to enhance the performance of photocatalysts in wastewater treatment applications.

3.4.3 Effect of catalyst dose. The cost of a catalyst may affect its application in the commercial sector. The effect of

Table 2 Performance evaluation of different photocatalysts for CR degradation

Photocatalyst	Light source	Lamp power (W)	Time (min)	Catalyst (g)	Pollutant concentration (g L^{-1})	Removal efficiency (%)	Quantum yield (molecules per photon)	Space-time yield (molecules per photon per mg)	Figure of merit; FOM (µmol L h^{-2} g^{-1} W^{-1})	Ref.
MnFe$_2$O$_4$/TA/ZnO	Vis	128	90	0.05	0.016	84.23	3.35×10^{-6}	6.70×10^{-8}	8.39×10^{-2}	47
NiFe$_2$O$_4$	Vis	128	75	0.005	0.005	85	2.03×10^{-6}	4.06×10^{-7}	2.44×10^{-1}	52
PANI/Fe^0 doped BiOC	Vis	500	120	0.1	0.05	79.91	7.63×10^{-7}	7.63×10^{-9}	2.87×10^{-3}	53
Cu based MOF	Vis	200	45	0.05	0.02	78	9.09×10^{-7}	1.82×10^{-8}	9.11×10^{-3}	54
Co$_{1-0.5}$Cu$_{0.5}$Fe$_2$O$_4$	Vis	500	90	0.01	0.01	71.37	9.09×10^{-8}	9.09×10^{-9}	2.28×10^{-3}	55
ZFCNM	Vis	50	75	0.075	0.01	98	3.01×10^{-6}	4.02×10^{-8}	2.42×10^{-2}	Current study

catalyst dose on the photodegradation efficiency of ZFCNM (1 : 1) against CR dye is shown in Fig. 8c. Important factors such as the morphological properties of the synthesized catalyst, the configuration of the reactor, the nature of the targeted pollutant, and light intensity help in an investigation of the optimum catalyst dosage. A catalyst dosage of 0.075 g gave the maximum photodegradation (98.63%) of CR dye. When there is a further increase in catalyst dose, it makes the solution turbid without any significant increase in photodegradation. This might be due to a multilayer stack of catalysts and difficulty in light penetration, which will hinder photodegradation.

3.4.4 Effect of dye concentration. The potency of a photocatalyst's kinetic efficiency is also influenced by the magnitude of the pollutant concentration. The impact of initial CR concentration on the photodegradation efficacy of the ZFCNM (1 : 1) composite is illustrated Fig. 8d. Notably, it was observed that the percentage degradation of CR dye diminishes with an increase in dye concentration. This trend can be attributed to the presence of a restricted number of active sites available for dye adsorption and the generation of hydroxyl ($^{\bullet}$OH) radicals within the reaction medium. Remarkably, the best photodegradation of CR dye *via* the ZFCNM composite was achieved at an initial pollutant concentration of 10 mg L^{-1}. Moreover, with an increase in dye concentration, the turbidity of solution increases, leading to reduced light penetration in contrast to more dilute concentrations. This decrease in light penetration adversely influences the photodegradation process.

3.4.5 Effect of light intensity. The intensity of a photon plays a key role in exciting an electron and producing an electron–hole pair to oxidize the organic pollutant molecules. By increasing light intensity from 25 to 50 W, the photodegradation increased from 74 to 98% of CR dye, as shown in Fig. 8e. This might be due to the increased numbers of high-energy photons that produce a higher number of $^{\bullet}$OH radicals. On the other hand, the incident light is also responsible for the rise in temperature of the reaction medium, which ultimately causes more free radicals.

3.5 Performance evaluation

Table 2 presents a comparative performance between the ZFCNM (1 : 1) composite (in this work) and reported photocatalysts applied to remove CR dye from an aqueous medium. Calculated QY values of synthesized ZF, CNM, and ZFCNM heterostructure were 1.21×10^{-6}, 9.21×10^{-7}, and 3.01×10^{-6} molecules per photon, respectively, whereas their corresponding SY values were 1.61×10^{-8}, 1.23×10^{-8}, and 4.02×10^{-8} molecules per photon per mg. Due to the effective separation of charges by the heterojunction, ZFCNM showed better photocatalytic performance under visible irradiation than pristine CNM or ZF for removing CR dye. It was also noted that the ZFCNM heterostructure had a higher FOM value of 2.42×10^{-2} µmol L h^{-2} g^{-1} W^{-1} compared with that of its pristine counterparts 9.66×10^{-3} µmol L h^{-2} g^{-1} W^{-1} (ZF) and 7.38×10^{-3} µmol L h^{-2} g^{-1} W^{-1} (CNM), which supports its actual application for the photodegradation of organic pollutants. Based on the computed performance metrics (FOM, QY, and STY values),
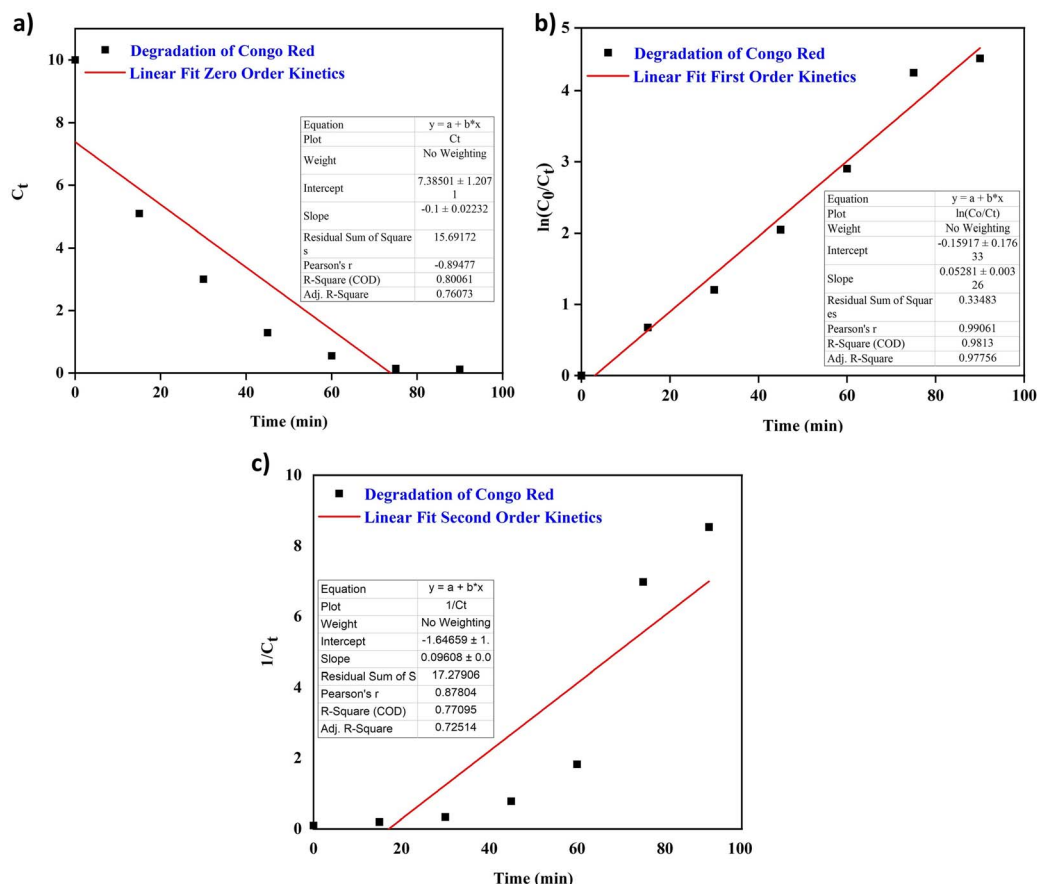
Fig. 9 CR degradation kinetics: (a) zero-order kinetics, (b) first-order kinetics and (c) second-order kinetics.

the photocatalytic performance of the ZFCNM composite can be ranked in descending order of ZFCNM > ZF > CNM. However, it is also worth noting that ZFCNM outperformed all reported catalysts for CR dye removal, except $MnFe_2O_4/TA/ZnO$ and $NiFe_2O_4$ with FOM values of 8.39×10^{-2} and 2.44×10^{-1} µmol L h^{-2} g^{-1} W^{-1}, respectively (Table 1). Effective visible light utilization, remarkably higher quantum yield, and a combination of low energy requirements make ZFCNM an effective photocatalyst for removing CR dye from water.

3.6 Kinetic studies

A comprehensive set of kinetic studies was conducted using various models to assess the effectiveness of the synthesized ZFCNM (1 : 1) nanocomposite, which was the top-performing photocatalyst compared to bare ZF and CNM for the photodegradation of CR dye.

The results are depicted in Fig. 9a–c. The kinetic analysis revealed that the first-order kinetic model, with an R^2 value of 0.9813, provided the best fit for the experimental data, compared to the zero-order ($R^2 = 0.80061$) and second-order ($R^2 = 0.77095$) models. This higher R^2 value indicates that the degradation of CR dye by the photocatalyst follows first-order kinetics, where the rate of degradation is directly proportional to the dye concentration. The superior fit of the first-order model suggests that it more accurately captures the

relationship between concentration and degradation over time, making it the most suitable model for describing the photocatalytic process in this study.

3.7 Scavenger test

To understand the photodegradation mechanism, Fig. 10 illustrates a strategy with various radical scavengers (t-BuOH, EDTA-2Na, and BQ) employed to evaluate the role of
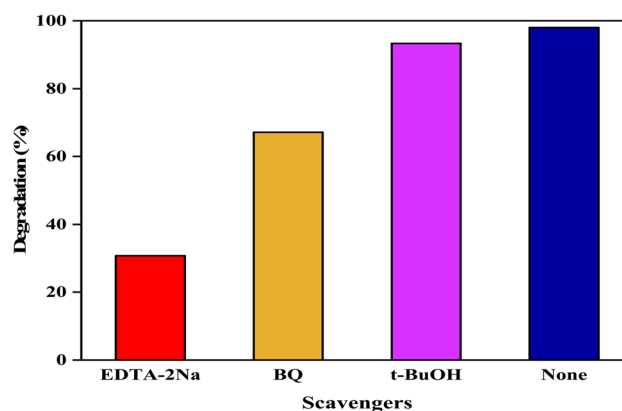

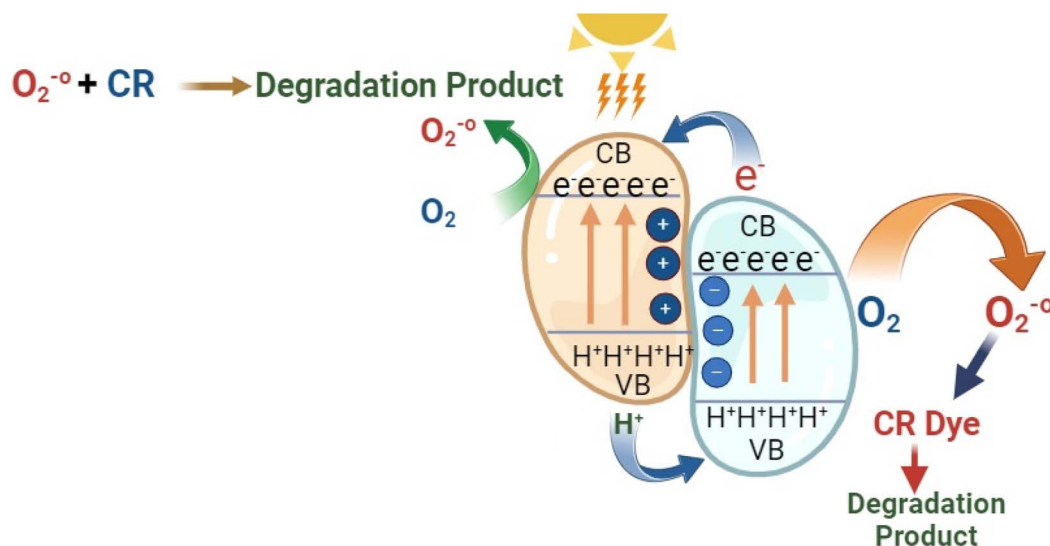**Fig. 10** Effect of different scavengers during photocatalytic degradation of CR dye by ZFCNM.

Fig. 11 The schematic diagram for the photocatalytic mechanism of the ZFCNM composite.

photogenerated reactive oxidative species ($^{\cdot}OH$, $^{\cdot}O_2^-$, and h^+) by the ZFCNM catalyst for CR dye degradation under visible irradiation. As can be seen, the photocatalytic efficiency of the ZFCNM composite was significantly suppressed in the presence of EDTA-2Na compared to that in the presence of BQ or t-BuOH inhibitors. Compared with bare photocatalysis (without the addition of radical scavengers), the photocatalytic efficiency of ZFCNM for CR dye removal was limited to 31.6, 55.25, and 84.75% in the presence of 1 mM EDTA-2NA, BQ, and t-BuOH, respectively. These findings indicate the dominant role of positive holes (h^+) and $^{\cdot}O_2^-$ radical species in the photodegradation process of CR dye. However, the participation of $^{\cdot}OH$ radicals plays a minor role in CR dye degradation by the ZFCNM heterostructure photocatalyst.

In this study, the ZFCNM composites, characterized by their high surface area, exhibit a superior capacity for the photodegradation of CR dye compared to ZF alone. This enhancement can be attributed to the effective separation of electron–hole pairs within the aqueous medium. A heterostructure is

formed through the integration of CNM and ZF, leading to a modified activation energy, as illustrated in Fig. 11. In this heterostructure, the conduction band (CB) of CNM demonstrates a higher electron intensity than that of ZF. Consequently, photogenerated electrons migrate from CNM to ZF until their Fermi levels coincide. This migration process results in the accumulation of electrons on the active sites of ZF and positive holes on the surface of CNM at the junction sites. As a consequence of this arrangement, the separation of photogenerated charge carriers occurs due to the influence of internal electrostatic fields within the heterojunction sites. The construction of a heterojunction structure between CNM and spinel ZF facilitates the effective separation of charge carriers, thereby leading to the high efficiency observed in the photocatalytic performance.

3.8 Reusability performance

Reusability and stability experiments were performed to check the multi-cycle usage of the synthesized photocatalysts. After six successive reaction cycles, a moderate decrease in activity was observed, with the efficiency remaining at 94%, as depicted in Fig. 12. These outcomes reflected that the synthesized ZFCNM composite has many benefits and could be used for industrial applications.

Fig. 12 Reusability of ZFCNM.

4. Conclusions

A highly effective and recyclable ZFCNM heterostructure photocatalyst has been successfully synthesized using a facile synthetic method. This photocatalyst demonstrated remarkable performance in the photodegradation of CR dye, even under mild reaction conditions. The strategic integration of CNM onto the ZF framework efficiently reduces electron–hole pair recombination within the ZFCNM heterostructure, consequently enhancing photocatalytic activity. The study also
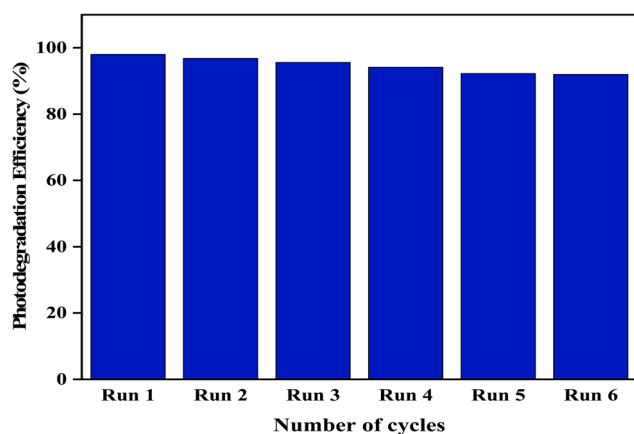
investigated the influence of different parameters, such as the weight ratio of CNM and ZF in the ZFCNM composite, on photocatalytic performance. The effect of medium pH, illumination time, intensity of visible light irradiation, and composite dosage for the photocatalytic degradation against different concentrations of CR dye have been studied. According to the results, ZFCNM offered an effective photodegradation efficiency of 98% and a quantum yield of 3.01×10^{-6} molecules per photon in 75 minutes at pH 5 and ambient temperature. Furthermore, the composition of CNM with ZF has many advantages, including reduced electron–hole recombination, efficient light absorption, and a controllable, well-structured porous framework with a narrow band gap. Considerable adsorption, good degradation capacity under mild reaction conditions, ease of handling, reusability and recovery, and environmental compatibility of the catalysts make this composite a promising candidate for industrial applications.

Data availability

Data will be made available on request.

Author contributions

Khalid Javed, Naseem Abbas, Muhammad Bilal, Syed Ali Raza Naqvi: methodology; formal analysis; investigation; writing – original draft. Hafiza Zahra Rab Nawaz, Mohamed Fawzy Ramadan and Abdulaziz A. Alshihri: formal analysis; writing – original draft. Yuling Zhang: formal analysis; investigation; Naseem Abbas, Syed Ali Raza Naqvi, Mohamed Fawzy Ramadan and Abdulaziz A. Alshihri: conceptualization; resources; supervision; funding acquisition; validation; writing-review and editing. Naseem Abbas: supervision; funding acquisition; validation; writing – review and editing. Khalid Javed, Naseem Abbas, & Syed Ali Raza Naqvi contributed equally to this work.

Conflicts of interest

The authors declare no competing interests'.

Acknowledgements

References

1 M. Daud, et al., Drinking water quality status and contamination in Pakistan, BioMed Res. Int., 2017, 2017(1), 7908183.

2 J. Li, et al., Metal-organic framework membranes for wastewater treatment and water regeneration, Coord. Chem. Rev., 2020, 404, 213116.

3 N. Yahya, et al., A review of integrated photocatalyst adsorbents for wastewater treatment, J. Environ. Chem. Eng., 2018, 6(6), 7411–7425.

4 A. Khan, et al., Synthesis of potent chitosan beads a suitable alternative for textile dye reduction in sunlight, J. Mater. Sci.: Mater. Electron., 2019, 30(1), 406–414.

5 A. Aziz, et al., Chitosan-zinc sulfide nanoparticles, characterization and their photocatalytic degradation efficiency for azo dyes, Int. J. Biol. Macromol., 2020, 153, 502–512.

6 R. Ranjith, et al., Green synthesis of reduced graphene oxide supported TiO_2/Co_3O_4 nanocomposite for photocatalytic degradation of methylene blue and crystal violet, Ceram. Int., 2019, 45(10), 12926–12933.

7 Z. Liu, et al., Aqueous tetracycline degradation by coal-based carbon electrocatalytic filtration membrane: effect of nano antimony-doped tin dioxide coating, Chem. Eng. J., 2017, 314, 59–68.

8 J. Cao, et al., Efficient charge transfer in aluminum-cobalt layered double hydroxide derived from Co-ZIF for enhanced catalytic degradation of tetracycline through peroxymonosulfate activation, Chem. Eng. J., 2020, 382, 122802.

9 X. Mo, et al., Boosting interfacial S-scheme charge transfer and photocatalytic H_2-production activity of 1D/2D WO_3/g-C_3N_4 heterojunction by molecular benzene-rings integration, J. Mater. Sci. Technol., 2023, 145, 174–184.

10 M. Y. Shah, et al., Synthesis of Mg–Co–LDH material and its applications for analyze the adsorption and desorption behavior of 4-nitrophenol, J. Iran. Chem. Soc., 2022, 19(2), 513–520.

11 Z. Zhang, et al., Bench-scale column evaluation of factors associated with changes in N-nitrosodimethylamine (NDMA) precursor concentrations during drinking water biofiltration, Water Res., 2019, 167, 115103.

12 J. Cao, et al., One-step synthesis of Co-doped UiO-66 nanoparticle with enhanced removal efficiency of tetracycline: Simultaneous adsorption and photocatalysis, Chem. Eng. J., 2018, 353, 126–137.

13 J. Grellier, et al., Exposure to disinfection by-products, fetal growth, and prematurity: a systematic review and meta-analysis, Epidemiology, 2010, 300–313.

14 K. Sharma and G. Kaushik, Pharmaceuticals: An Emerging Problem of Environment and Its Removal Through Biodegradation, Environ. Microbiol. Biotechnol., 2021, 267–292.

15 E. A. Serna-Galvis, et al., Degradation of seventeen contaminants of emerging concern in municipal wastewater effluents by sonochemical advanced oxidation processes, Water Res., 2019, 154, 349–360.

16 Y. Tan, et al., Fabrication of an Au25-Cys-Mo Electrocatalyst for Efficient Nitrogen Reduction to Ammonia under Ambient Conditions, Small, 2021, 17(21), 2100372.

17 F. Liu, et al., Heterogeneous activation of peroxymonosulfate by cobalt-doped MIL-53 (Al) for efficient tetracycline degradation in water: Coexistence of radical and non-radical reactions, J. Colloid Interface Sci., 2021, 581, 195–204.

18 L. Ao, et al., Enhanced nitrate removal by micro-electrolysis using Fe^0 and surfactant modified activated carbon, Chem. Eng. J., 2019, 357, 180–187.

19 Z.-h. Yang, et al., Mn-doped zirconium metal-organic framework as an effective adsorbent for removal of tetracycline and Cr (VI) from aqueous solution, Microporous Mesoporous Mater., 2019, 277, 277–285.

20 X. Liu, et al., Adsorption and desorption of U (VI) on different-size graphene oxide, Chem. Eng. J., 2019, 360, 941–950.

21 A. R. Zare, A. A. Ensafi and B. Rezaei, An impedimetric biosensor based on poly (l-lysine)-decorated multiwall carbon nanotubes for the determination of diazinon in water and fruits, J. Iran. Chem. Soc., 2019, 16(12), 2777–2785.

22 M. Fu, et al., Sol–gel preparation and enhanced photocatalytic performance of Cu-doped ZnO nanoparticles, Appl. Surf. Sci., 2011, 258(4), 1587–1591.

23 E. M. Dias and C. Petit, Towards the use of metal–organic frameworks for water reuse: a review of the recent advances in the field of organic pollutants removal and degradation and the next steps in the field, J. Mater. Chem. A, 2015, 3(45), 22484–22506.

24 N. A. Khan, Z. Hasan and S. H. Jhung, Adsorptive removal of hazardous materials using metal-organic frameworks (MOFs): a review, J. Hazard. Mater., 2013, 244, 444–456.

25 K. H. Ng and C. K. Cheng, Photo-polishing of POME into CH_4-lean biogas over the UV-responsive ZnO photocatalyst, Chem. Eng. J., 2016, 300, 127–138.

26 D. Channei, et al., Photocatalytic degradation of methyl orange by CeO_2 and Fe-doped CeO_2 films under visible light irradiation, Sci. Rep., 2014, 4(1), 1–7.

27 Q. Song and Z. J. Zhang, Controlled synthesis and magnetic properties of bimagnetic spinel ferrite $CoFe_2O_4$ and $MnFe_2O_4$ nanocrystals with core–shell architecture, J. Am. Chem. Soc., 2012, 134(24), 10182–10190.

28 X. Zhang, et al., Modification of WO_3 photoanode with NiFe-LDHs nanosheets array for efficient Photoelectrocatalytic removal of tetracycline, Appl. Surf. Sci., 2023, 622, 156977.

29 H. Gupta, P. Paul and N. Kumar, Synthesis and characterization of $DHA/ZnO/ZnFe_2O_4$ nanostructures for biomedical imaging application, Procedia Mater. Sci., 2014, 5, 198–203.

30 X. Li, et al., Double-shell architectures of $ZnFe_2O_4$ nanosheets on ZnO hollow spheres for high-performance gas sensors, ACS Appl. Mater. Interfaces, 2015, 7(32), 17811–17818.

31 H. Zhu, et al., Microemulsion-based synthesis of porous zinc ferrite nanorods and its application in a room-temperature ethanol sensor, Nanotechnology, 2008, 19(40), 405503.

32 X. Zhou, et al., Template-free synthesis of hierarchical $ZnFe_2O_4$ yolk–shell microspheres for high-sensitivity acetone sensors, Nanoscale, 2016, 8(10), 5446–5453.

33 Q. Zhao, et al., F-doped zinc ferrite as high-performance anode materials for lithium-ion batteries, New J. Chem., 2022, 46(20), 9612–9617.

34 N. Yadav, et al., Impact of collected sunlight on $ZnFe_2O_4$ nanoparticles for photocatalytic application, J. Colloid Interface Sci., 2018, 527, 289–297.

35 T. B. Nguyen, C. Huang and R.-a. Doong, Photocatalytic degradation of bisphenol A over a $ZnFe_2O_4/TiO_2$ nanocomposite under visible light, Sci. Total Environ., 2019, 646, 745–756.

36 M. Su, et al., Mesoporous zinc ferrite: synthesis, characterization, and photocatalytic activity with H_2O_2/visible light, J. Hazard. Mater., 2012, 211, 95–103.

37 C.-J. Du, et al., Prussian blue analogue $K_2Zn_3[Fe(CN)_6]_2$ quasi square microplates: large-scale synthesis and their thermal conversion into a magnetic nanoporous $ZnFe_{2-x}O_4$–ZnO composite, CrystEngComm, 2013, 15(48), 10597–10603.

38 X. Zhang, et al., MOF-derived magnetically recoverable Z-scheme $ZnFe_2O_4/Fe_2O_3$ perforated nanotube for efficient photocatalytic ciprofloxacin removal, Chem. Eng. J., 2022, 430, 132728.

39 H.-C. Zhou, J. R. Long and O. M. Yaghi, Introduction to metal–organic frameworks, Chem. Rev., 2012, 112(2), 673–674.

40 Y. Qiu, et al., Hollow Ni/C microspheres derived from Ni-metal organic framework for electromagnetic wave absorption, Chem. Eng. J., 2020, 383, 123207.

41 N. Abbas, et al., The photocatalytic performance and structural characteristics of nickel cobalt ferrite nanocomposites after doping with bismuth, J. Colloid Interface Sci., 2021, 594, 902–913.

42 M. Shaban, et al., Photocatalytic degradation and photo-Fenton oxidation of Congo red dye pollutants in water using natural chromite—response surface optimization, Appl. Water Sci., 2017, 7, 4743–4756.

43 M. Bilal, et al., Designing of stable copper ferrite-doped metal–organic framework heterostructure for improved visible light-induced photodegradation of 4-nitrophenol in water, Int. J. Environ. Sci. Technol., 2024, 1–14.

44 M. Mehdipour, H. Shokrollahi and A. Bahadoran, Investigating the exchange-coupling interaction in nanostructure composite particles of $SrFe_{12}O_{19}$ and $ZnFe_2O_4$, J. Electron. Mater., 2014, 43, 4282–4288.

45 S. A. Younis and Y. M. Moustafa, Synthesis of urea-modified $MnFe_2O_4$ for aromatic micro-pollutants adsorption from wastewater: mechanism and modeling, Clean Technol. Environ. Policy, 2017, 19(2), 527–540.

46 H. Ramezanalizadeh and F. Manteghi, Immobilization of mixed cobalt/nickel metal-organic framework on a magnetic $BiFeO_3$: A highly efficient separable photocatalyst for degradation of water pollution, J. Photochem. Photobiol., A, 2017, 346, 89–104.

47 B. Boutra, et al., Magnetically separable $MnFe_2O_4/TA/ZnO$ nanocomposites for photocatalytic degradation of Congo Red under visible light, J. Magn. Magn. Mater., 2020, 497, 165994.

48 N. Ali, Photocatalytic degradation of congo red dye from aqueous environment using cobalt ferrite nanostructures: development, characterization, and photocatalytic performance, *Water, Air, Soil Pollut.*, 2020, **231**(2), 1–16.

49 A. Rolston, Social changes affect water quality too, *Nature*, 2016, **536**(7617), 396.

50 D. Chen, *et al.*, Photocatalytic degradation of organic pollutants using TiO_2-based photocatalysts: A review, *J. Cleaner Prod.*, 2020, **268**, 121725.

51 T. Nguyen, *et al.*, Effect of pH on the adsorption behaviour of Congo Red Dye on the Mg-Al layered double hydroxide, *IOP Conf. Ser.: Mater. Sci. Eng.*, 2020, 022077.

52 M. B. Taj, *et al.*, Bioconjugate synthesis, phytochemical analysis, and optical activity of $NiFe_2O_4$ nanoparticles for the removal of ciprofloxacin and Congo red from water, *Sci. Rep.*, 2021, **11**(1), 5439.

53 R. Tanwar, *et al.*, Photocatalytic activity of PANI/Fe^0 doped BiOCl under visible light-degradation of Congo red dye, *J. Photochem. Photobiol., A*, 2017, **333**, 105–116.

54 R. Foulady-Dehaghi and S. Sohrabnezhad, Hybridization of Schiff base network and amino functionalized Cu based MOF to enhance photocatalytic performance, *J. Solid State Chem.*, 2021, **303**, 122549.

55 V. Kirankumar, B. Hardik and S. Sumathi, Photocatalytic degradation of congo red using copper substituted cobalt ferrite, *IOP Conf. Ser.: Mater. Sci. Eng.*, 2017, 026102.